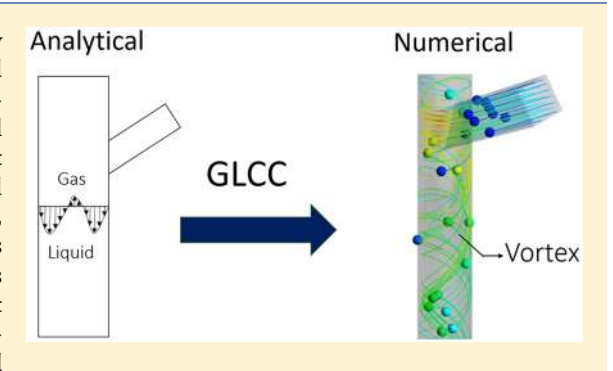


Numerical Simulation of a Natural Gas Cylindrical Cyclone Separator **Using Computational Fluid Dynamics**

Juan Sebastian Cornejo Caceres, Datalia Prieto, Arto German Gonzalez, German Gonzalez, and Arlex Chaves-Guerrero

GIEMA Laboratory, Universidad Industrial de Santander, Santander 680005, Colombia

ABSTRACT: Gas-liquid separators are one type of surface facility among those used in oil fields. In this paper, the study of gas-liquid separation in a cylindrical cyclone separator (GLCC) using computational fluids dynamics was carried out. The multiphase mixture model and the $k-\varepsilon$ turbulence model in an air-water mixture with different geometries of the separator varying the inlet angle from 27° to 36° and 45° were used. Later, variables for the volumetric fraction, velocity, and pressure drop in the separator were studied. Finally, a natural gas mixture from a Colombian oil field was simulated using a species transport model. The results showed that a 36° inlet is the most suitable for the separation process due to its capacity to form a highintensity swirl without produced liquid carry over. Also, it was found



that the centrifugal separator could be a suitable alternative compared with conventional gravitational gas-liquid separators.

INTRODUCTION

To make natural gas suitable for merchandising, it is necessary to separate some components that can generate problems during its transport and use. One of the processes applied is the separation of the heavier components or condensates with the purpose to have the gas satisfy the regulations of marketing and transportation. Actually, the removal of condensates from natural gas is typically carried out in gravitational separators which have disadvantages in that they are heavy, are big, and have relatively high maintenance costs. An alternative to this problem may be the use of the gas-liquid cylindrical cyclone (GLCC) separator, which is compact and has a simple geometry and economical maintenance.2 The GLCC uses, in addition to the gravitational force, centrifugal forces which separate the heavier phase from the lighter one. For generating the centrifugal forces, a stream enters tangentially to the GLCC walls, forming a swirl which gives the energy for the separation process.3 Compact cyclonic separators have been used in primary separation, in well test metering systems, for control of the gas-liquid ratio for multiphase meters, pumps, and desanders, in gas scrubbing for flare gas, and for external preseparation upstream of existing conventional separators. Currently, GLCC separators are being considered for a variety of subsea applications and will soon be installed as part of a subsea multiphase pumping system.4

The GLCC separators were developed by the Tulsa University Separation Technology Projects team in 1995, and since then, different studies have been developed around the relevant parameters of design and operation. 5,6 For instance, Yang et al. studied the residence time of the liquid phase in a cyclonic separator, obtaining that the liquid

residence time decreases with the increasing of droplets loading, while the decrease is smaller when the inlet velocity increases. On the other hand, the liquid residence time increases with the cylinder diameter. Geometric parameters such as shape, size, angle, and number of inlets were analyzed using computational fluid dynamics (CFD) to evaluate the geometry effects on the liquid carry-over and gas carry-under. The results of the simulation showed that the inlets of the gasliquid mixture must be placed 10 cm above half the axial length of the separator, with inclination angles between 27° and 40°. Also, it was found that multiple inlets are convenient for systems where the density difference between the phases is considerably high, as is the case of air-water or air-glycerin mixtures and that a single entry was convenient for blends in which the density of the gas phase increases.^{8,9}

Recently, Yue et al.¹⁰ developed an experimental and numerical study about the upper swirling liquid film (USLF) in GLCC separators for mixtures of water, glycerin, and therminol-55 at four flow regimes, i.e., swirling flow, churn flow, annular flow, and ribbon flow. The authors found that the action of the USLF on the liquid carry-over phenomenon can be divided into three stages, namely, safety stage, the deteriorating stage, and the stable stage; they correspond to the flow regimes of swirl flow, churn flow, and annular flow, respectively. Alternative uses of the GLCC separator have also recently been studied, such as the cyclone adaptation to the

March 4, 2019 Received: Revised: July 4, 2019 Accepted: July 8, 2019 Published: July 8, 2019

[‡]GMPH Laboratory, Universidad Industrial de Santander, Santander 680005, Colombia

gravitational separator inlet, operating as pre-separation devices, 11 and the gas—liquid mixtures analysis with a high content of solid contaminants. In the last case, the multiphase flow, as well as the erosion produced by the solid particles (sand), were studied. 12

Given that the swirling flow will be in contact with the walls of the mechanism, the geometry and dimensions of the GLCC are critical factors to take into account in the design of these separators.¹³ Among the design aspects, variables include the diameter to length ratio of the cylindrical vessel, the dimensions, and the angle of the inlet; further, the outlets have to be placed correctly. 14,15 A proper design of these aspects can lead to avoiding the liquid carry-over and the gas carry-under, two operational problems that can generate a poor separation of the phases.¹⁴ The sizing of the inlet is highly important owing to that it controls the vortex intensity. The inlet must be placed just above the liquid level. In the studies it was found that the inlet has to have an angle of at least 27° , so that the fluids can stratify; added to that, a rectangular shape inlet is recommended when the gas is the continuum phase. Additionally, when the quantity of liquid is low, a nonconvergent inlet shows better results.16

Despite the advances in the study of GLCC separators, most of the mixtures used were air—water at high purity conditions. However, there is a potential opportunity to use GLCC in the separation of the phases present in small deposits of natural gas where compact equipment is required because it generates low maintenance costs. The understanding of the fluid dynamics inside the separator is accomplished by the use of mechanical models found in specialized literature. S,15,17 Furthermore, due to the complexity of the mathematical models of swirling flows, the solution of this must be obtained using computational fluid dynamics (CFD). 18

The objective of this study was to determine the feasibility of using a GLCC separator to separate the heavy components of natural gas as an alternative to the use of gravitational separators. The technique used to solve physical models was CFD, specifically through the tool ANSYS Fluent 18.0. First, an air-water mixture was used in different geometries of the separator (obtained varying the inlet angle from 27° to 36° and 45°) to select the one which has a vortex with favorable characteristics for phase separation. Therefore, variables such as the volumetric fraction, velocity fields, and pressure drop were determined. The results of these variables were compared with the work of Hreiz et al., 23 which performed the fluid dynamics analysis of different turbulence models for different fluid mixtures in a GLCC separator and compared them with the experimental data obtained by Erdal.²⁴ Next, a natural gas mixture from a Colombian oil field called Cusiana was simulated to have a grasp of the fluid-dynamic behavior of the gas in the separator and to evaluate this device as an alternative for the primary treatment of natural gas.

MATHEMATICAL MODEL

Transport Equations. The transport equations of continuity and momentum for an incompressible and multiphase flow in the GLCC are provided in eqs 1 and 2. This mathematical model does not include mechanisms of mass and energy transfer, only phase separation.

$$\frac{\partial \rho_m}{\partial t} + \vec{\nabla} \cdot (\rho_m \vec{v}_m) = 0 \tag{1}$$

$$\frac{\partial(\rho_m\vec{v}_m)}{\partial t} + \vec{\nabla}\cdot(\rho_m\vec{v}_m\vec{v}_m) =$$

$$-\vec{\nabla}p + \vec{\nabla}\cdot\vec{\vec{T}} + \rho_{m}\vec{g} + \vec{F} - \vec{\nabla}\cdot\left(\sum_{k=1}^{n}\alpha_{k}\rho_{k}\vec{v}_{\mathrm{dr},k}\vec{v}_{\mathrm{dr},k}\right)$$
(2)

In eq 1 $\vec{v}_{\rm m}$ is the average mass velocity vector and $\rho_{\rm m}$ is the average specific mass which are defined as

$$\rho_m = \sum_{k=1}^n \alpha_k \rho_k \tag{3}$$

$$\vec{v}_m = \frac{\sum_{k=1}^n \alpha_k \rho_k \vec{v}_k}{\rho_m} \tag{4}$$

with α_k representing the volumetric fraction. On the other side in eq 2, p is the static pressure and \vec{T} is the viscous stress tensor for a Newtonian fluid:

$$\vec{\vec{T}} = \mu \left[(\vec{\nabla} \vec{v}_m + \vec{\nabla} \vec{v}_m^T) - \frac{2}{3} \vec{\nabla} \cdot \vec{v}_m \vec{\vec{I}} \right]$$
(5)

where $\rho_{m}\vec{g}$ is the gravitational body force, and \vec{F} represents additional external body forces that could interact with the fluid. In eq 5, μ is the dynamic viscosity and \vec{l} is the identity tensor

For validation purposes of the air-water mixture with the experimental data, the multiphase flow in the GLCC was modeled using the Euler-Euler approach which is taken into account by the fifth term on the right side of eq 2. Eulerian description of fluid flow is based on the notion of pseudocontinuum, i.e., the approach defines a point volume fraction for each phase which represents the probability of a particular phase to be present at that point in multiple realizations of flow. The same pressure field is shared between all of the phases. The force interaction between phases is incorporated through various effective "volumetric" force functions, such as drag force, lift force, virtual mass effect, among others (defined as net force between phases per unit volume). 19,20 This model considers that the phases have different velocities and that a local equilibrium between them should be reached over a short spatial length scale. The slip velocity (\vec{v}_{pq}) is defined as the velocity of a secondary phase (p) relative to the velocity of the primary phase (q)

$$\vec{v}_{pq} = \vec{v}_p - \vec{v}_q \tag{6}$$

The drift velocity $(\vec{v}_{dr,k})$ for any phase (k) is defined as

$$\vec{v}_{\mathrm{dr},k} = \vec{v}_k - \vec{v}_m \tag{7}$$

The drift and slip velocity are connected as follows:

$$\vec{v}_{\text{dr},p} = \vec{v}_{pq} - \sum_{k=1}^{n} \frac{\alpha_k \rho_k \vec{v}_{qk}}{\rho_m}$$
(8)

To describe the relative velocity, the model developed by Manninen et al.²¹ was used. The form of the slip velocity is given by

$$\vec{v}_{pq} = \frac{\tau_p}{f_{\text{drag}}} \frac{\rho_p - \rho_m}{\rho_p} \vec{a} \tag{9}$$

where τ_n is the droplet relaxation time:

$$\tau_p = \frac{\rho_p d_p^2}{18\mu_q} \tag{10}$$

In this equation, *d* is the diameter of the droplets of secondary phase p, and \vec{a} is the secondary-phase droplet's acceleration. The drag function f_{drag} is taken from Schiller and Naumann.²²

$$f_{\text{drag}} = \begin{cases} 1 + 0.15 \text{Re}^{0.687} & \text{Re} \le 1000\\ 0.0183 \text{Re} & \text{Re} > 1000 \end{cases}$$
 (11)

and the acceleration \vec{a} is defined as

$$\vec{a} = \vec{g} - (\vec{v}_m \cdot \vec{\nabla}) \vec{v}_m - \frac{\partial \vec{v}_m}{\partial t}$$
(12)

Species Transport. Unlike the air—water mixture in which there are two components in clearly differentiated phases, natural gas is a multi-component mixture, whose transport phenomena can vary for each species. In this case, the species transport model is used, which predicts the local mass fractions of each species, y_{ij} through the solution of a convectiondiffusion equation for the ith species. This equation has the general form of eq 13.

$$\frac{\partial(\rho Y_i)}{\partial t} + \vec{\nabla} \cdot (\rho \vec{v} Y_i) = -\vec{\nabla} \cdot \vec{J}_i \tag{13}$$

An equation of this form is solved for N-1 species, where N is the total number of species present in the system. Since the mass fraction of the species must sum to unity, the Nth mass fraction is determined as one (1) minus the sum of the N-1 solved mass fractions. J_i is the diffusion flux of species i, which arises due to gradients of concentration. Equation 14 shows the calculation of the mass diffusion.

$$\vec{J}_i = -\left(\rho D_{i,m} + \frac{\mu_t}{Sc_t}\right) \vec{\nabla} Y_i \tag{14}$$

where

$$Sc_t = \frac{\mu_t}{\rho D_t} \tag{15}$$

and where μ_t is the turbulent viscosity and D_t is the turbulent

Turbulence Model. Turbulence is the unstable and irregular movement of the fluid in which the transported quantities as the mass and momentum fluctuate through space and time. Additionally, the mixture properties, represented as the specific mass and velocity, show random changes where eddies can be recognized. Theoretically, turbulent flows can be simulated with the numerical solution of the Navier-Stokes equations; however, this requires a huge computational cost which is not practical for industrial flows. To reduce the computational cost, the equations can be averaged. For solving this system, the addition of the turbulence models is necessary. The $k-\varepsilon$ Realizable turbulence model was used in this work. This turbulence model is robust and has reasonable precision. Hreiz et al.²³ developed a work in which they compared the Reynolds averaged Navier-Stokes (RANS), unsteady Reynolds averaged Navier-Stokes (URANS), and large eddy simulation (LES) turbulence models in the two-phase flow inside a GLCC separator. These turbulence models were validated with the experimental data presented by Erdal.²⁴ The results showed that although the LES methodology was closer

to the experimental behavior, as expected, the $k-\varepsilon$ Realizable turbulence model also represented the experimental data adequately and has a lower computational cost, compared with LES. Additionally, it is the most common model for industrial applications including for flows with rotating fluids which are present in the GLCC. The turbulence model is described by eqs 16 and 17 which represent the balance of turbulent kinetic energy (k) and dissipation of turbulent energy (ε) , respectively.

$$\begin{split} \frac{\partial \rho k}{\partial t} + \frac{\partial}{\partial x_{i}} \rho k \vec{v}_{i} &= \frac{\partial}{\partial x_{j}} \left[\left(\mu + \frac{\mu_{t}}{\sigma_{k}} \right) \frac{\partial k}{\partial x_{j}} \right] \\ &+ G_{k} + G_{b} - \rho \varepsilon - Y_{M} + S_{k} \qquad (16) \\ \frac{\partial \rho \varepsilon}{\partial t} + \frac{\partial}{\partial x_{i}} \rho \varepsilon \vec{v}_{i} &= \frac{\partial}{\partial x_{j}} \left[\left(\mu + \frac{\mu_{t}}{\sigma_{\varepsilon}} \right) \frac{\partial \varepsilon}{\partial x_{j}} \right] \\ &+ C_{1\varepsilon} \frac{\varepsilon}{k} (G_{k} + C_{3\varepsilon} G_{b}) - C_{2\varepsilon} \rho \frac{\varepsilon^{2}}{k} + S_{\varepsilon} \end{split}$$

where G_k represents the generation of turbulence kinetic energy due to the mean velocity gradients. G_b is the generation of turbulence kinetic energy due to buoyancy. Y_M is the contribution of the fluctuating dilatation in compressible turbulence to the overall dissipation rate. C_{1e} , C_{2e} , and C_{3e} are constants. σ_k and σ_ϵ are the turbulent Prandtl number for k and ε , respectively. S_k and S_{ε} are user-defined source terms; in this case, the two terms are zero. The turbulent viscosity μ_t is computed by combining k and ε .

$$\mu_t = \rho C_\mu \frac{k^2}{\varepsilon} \tag{18}$$

where $C_{1\varepsilon}$ = 1.44, $C_{2\varepsilon}$ = 1.92, C_{μ} = 0.09, σ_k = 1.0, and σ_{ε} = 1.3. These values were suggested by Versteeg and Malalasekera.²⁵ Equation 16 shows the first variable, the turbulence kinetic energy, k, and eq 17 shows the dissipation of the turbulence kinetic energy, ε . An advantage of the realizable $k-\varepsilon$ turbulence model is that it provides improved predictions for the spreading rate of both planar and round jets. It also exhibits high performance for flows involving rotation, boundary layers under strong adverse pressure gradients, separation, and recirculation. ²⁶ For solving the region near the wall, standard wall functions were used, based on the work of Launder and Spalding.²⁷ The law-of-the-wall for mean velocity is

$$U^* = \frac{1}{\kappa} \ln(Ey^*) \tag{19}$$

where U^* is the dimensionless velocity (eq 20) and y^* is the dimensionless distance from the wall (eq 21).

$$U^* \equiv \frac{U_p C_\mu^{1/4} k_p^{1/2}}{\tau_w / \rho} \tag{20}$$

$$y^* \equiv \frac{\rho C_{\mu}^{1/4} k_p^{1/2} y_p}{\mu} \tag{21}$$

 κ is the von Kármán constant, E is an empirical constant, U_n is the mean velocity of the fluid at the wall-adjacent cell centroid (P), k_p is the turbulence kinetic energy at the walladjacent cell centroid (P), and y_p is the distance from the centroid of the wall—adjacent cell to the wall (P).

The law-of-the-wall for species can be expressed for constant property flow with no viscous dissipation:

$$Y^* \equiv \frac{(Y_{i,w} - Y_i)\rho C_{\mu}^{1/4} k_p^{1/2}}{J_{i,w}} = \begin{cases} Scy^* & (y^* < y_c^*) \\ Sc_t \left[\frac{1}{\kappa} \ln(Ey^*) + P_c \right] & (y^* > y_c^*) \end{cases}$$
(22)

where $J_{i,w}$ is the diffusion flux of species i at the wall. P_c and y_c * are in function of the Schmidt number.

Problem Description. The GLCC dimensions were taken from the geometry proposed by Hreiz et al. ¹⁸ shown in Figure 1a. Additionally, two variations are made to the inlet, increasing its angle from 27° to 36° and 45° (Figure 1b).

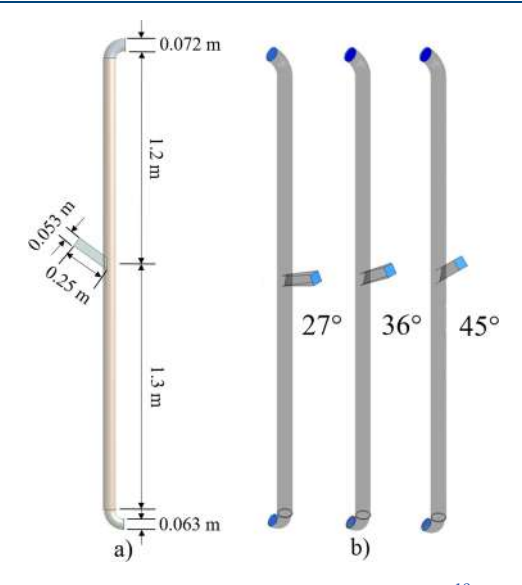


Figure 1. (a) GLCC dimensions taken from Hreiz et al. 18 and (b) the proposed geometries for this work.

The numerical calculations are divided into two stages. The first uses the multiphase model to validate the separation of the air—water phases, and the second is the species monitoring of a natural gas mixture from a Colombian field called Cusiana. Its composition and principal properties as density and viscosity of each component are shown in the Table 1.²⁸

Table 1. Natural Gas Inlet Composition

component	molar percent (%)	density (kg/m³)	viscosity (cP)
methane	82.19	0.7541	9.97×10^{-3}
ethane	10.43	1.426	8.209×10^{-3}
propane	3.59	2.116	7.103×10^{-3}
butane	1.02	615.4	0.2346
pentane	0.12	658	0.3154
hexane	0.02	691.3	0.4463
nitrogen	0.65	1.314	0.01648
carbon dioxide	1.97	2.079	0.01258

The boundary conditions were established for every surface in the domain, namely, the inlet, the bottom and superior outlets, and the wall. The used values for the air—water mixture were taken from the study of Hreiz et al. ¹⁸ These conditions are specified in the Table 2.

For solving the steady convection—diffusion equation, the Quadratic Upstream Interpolation for Convective Kinematics

Table 2. Boundary Conditions

substance	surface	condition	val	ue	units
air-water	inlet	velocity	air water	3.46 0.69	m/s
	outlets walls	pressure (static) no slip	0		Pa
natural gas	inlet outlets walls	velocity pressure (static) no slip	3.46 0		m/s Pa

(QUICK), presented by Patankar,²⁹ was used. This is a higher-order differencing scheme that considers a three-point upstream weighted quadratic interpolation for the cell face values. This scheme is used to solve convection—diffusion equations using second-order central difference for the diffusion term, and for the convection term, the scheme is third-order accurate in space and first-order accurate in time. The pressure discretization was performed with the PRESTO (PREssure STaggering Option) scheme, which, unlike the standard discretization method that interpolates the pressure on the faces using the cell center values, calculates pressure on each face. This is possible using staggered grids where velocity and pressure variables are not "co-located".²⁹

■ RESULTS AND DISCUSSION

The results are divided into three parts, namely, (i) the numerical tests of mesh independence; (ii) the validation of the models that represent the physical phenomenon by means the comparison with experimental data; and (iii) the flow analysis of GLCC separator by numerical simulations for the air—water and natural gas mixtures.

Mesh Independence Test. Seven computational meshes were generated using ANSYS—Meshing software: starting from a coarse mesh (A) and progressively increasing the number of elements according to Table 3. The refining ratio of the meshes was based on the decrease in the size of the mesh elements, approximately 1.5 times each time and also as a function of the inflation in the regions near the wall.

The tetrahedrons that composed the mesh were generated with the best characteristics in the main cylinder, and hexahedrons were generated in the inlet. The mesh has a refinement of three layers in the walls. Figure 2, left, shows the overall velocity profile at 1, 1.5, and 1.3 m from the bottom of the GLCC separator as a function of mesh elements. It is observed that, from the mesh E (265251 elements), an asymptotic behavior is observed in all the points. Subsequently, the mesh E was refined near to the wall, resulting in the final number of elements of Figure 2, right.

Model Validation. The validation was made by comparing the results obtained from the simulation with the experimental study data obtained by Hreiz et al., ¹⁸ who developed a complete experimental study that allowed them to evaluate the performance of the GLCC through the visualization of the flow patterns produced at different operating conditions and by changes made in the geometry of the equipment. The experimental separator consisted of translucent equipment built of poly(methyl methacrylate) (Plexiglas) with 72 mm of internal diameter and 2.5 m of height. The authors used air as the gas phase and three different fluids for the liquid phase, i.e., tap water, a 30% aqueous solution of carboxymethyl cellulose sodium salt which acts as a viscosifier, and a 0.05% aqueous solution of polyethylene glycol sorbital monooleate, a

Table 3. Elements of the Meshes Used in the Numerical Independence Test

mesh	A	В	С	D	E	F	G
elements	53312	93054	127184	180090	265251	416406	721364
7 6 [m] A A A A A A A A A A A A A A A A A A A	000 300000 40000 Number of	→1 m →1.3 m →1.15 m	12/184			410406 Case 27° 36° 45°	Number of elements 289424 288316 287106
					Transversal cut		

Figure 2. Mesh independence test (left) and effect of the mesh refinement in the walls.

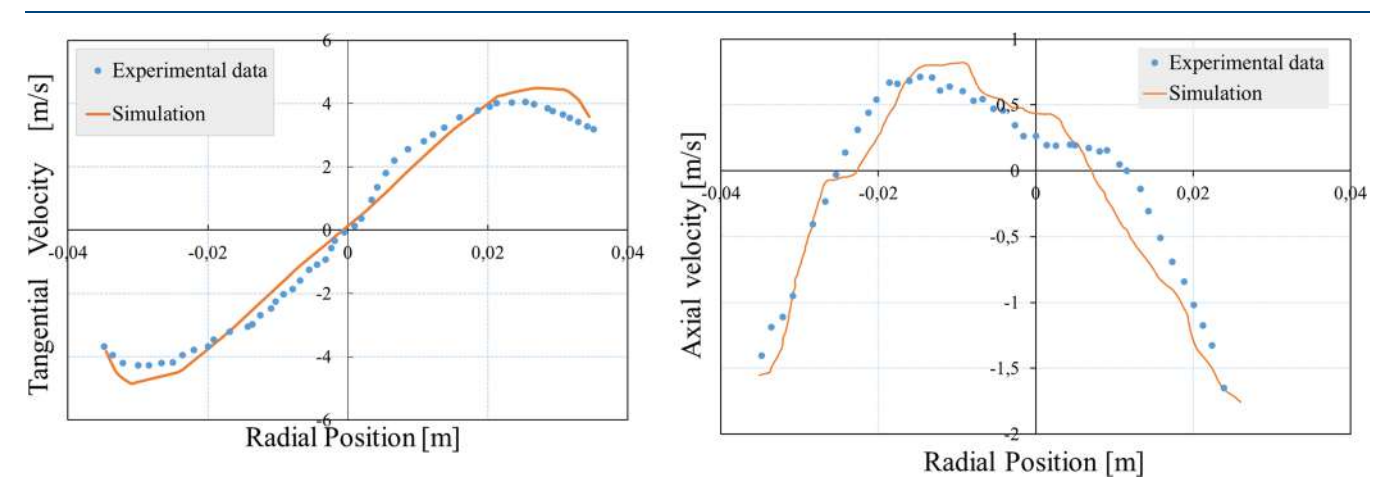


Figure 3. Tangential and axial velocity. Comparison between simulations and experimental data by Erdal. 23,24

surfactant foam that decreases the surface tension of the tap water. The maximum relative pressure was 0.8 bar (close to atmospheric pressure), and the maximum flow rate was 550 m³/h. The experiments showed the effect of the flow patterns and the geometric factors of the device on the liquid carry-over and the gas carry-under. On the other hand, the experimental data of radial and tangential velocity were confirmed by comparison with the study carried out by Erdal.²⁴ The experimental measurements were the axial and tangential velocity in the cyclone at 0.6 m below the inlet. According to Figure 3, the chosen mathematical models reproduce the fluiddynamic properly owing to that the experimental data and the simulation results have the same behavior and their values show a standard deviation average of 0.26 m/s. Further, a comparison between the simulations results of the mesh with and without refinement is made in Figure 4. The values of the nonrefined mesh differ broadly from the experimental data, showing the importance of a proper meshing in order to have more accurate results.

Air—Water Mixture. The phase separation is caused by the centrifugal forces which depend on the swirl intensity generated in the GLCC. Thus, the swirl intensity was related to the angular velocity measured at 0.6 m above the inlet. Figure 5a shows the angular velocity as a function of the radial position for each geometry. From this plot, it is possible to appreciate that when the inlet angle increases, the angular velocity decreases, leading to a poor swirl intensity. Hence, the separation capacity of a cyclone with a more significant inlet angle would be smaller; in this case, the geometry with an angle of 27° can make a swirl intensity up to 17% and 66% higher than the other two geometries, respectively. Figure 5b shows the velocity contours which exhibit the swirl formation with a higher velocity at the inlet due to the fact that it is designed with a tapered area which increases the velocity.

Figure 6 shows the pressure contours for each geometry as a function of its length. The pressure drop for each case is nearly the same; however, in the inlet region, it is different. This region shows an increase in the pressure for the three cases as a

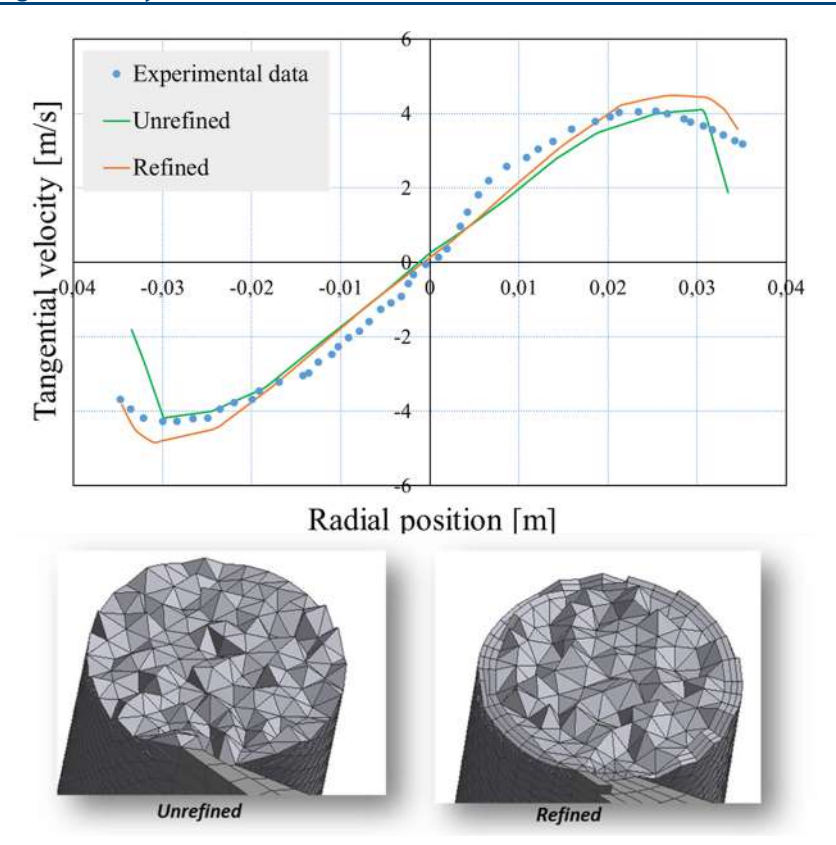


Figure 4. Tangential velocity with and without mesh refinement and experimental data by Erdal. ^{23,24}

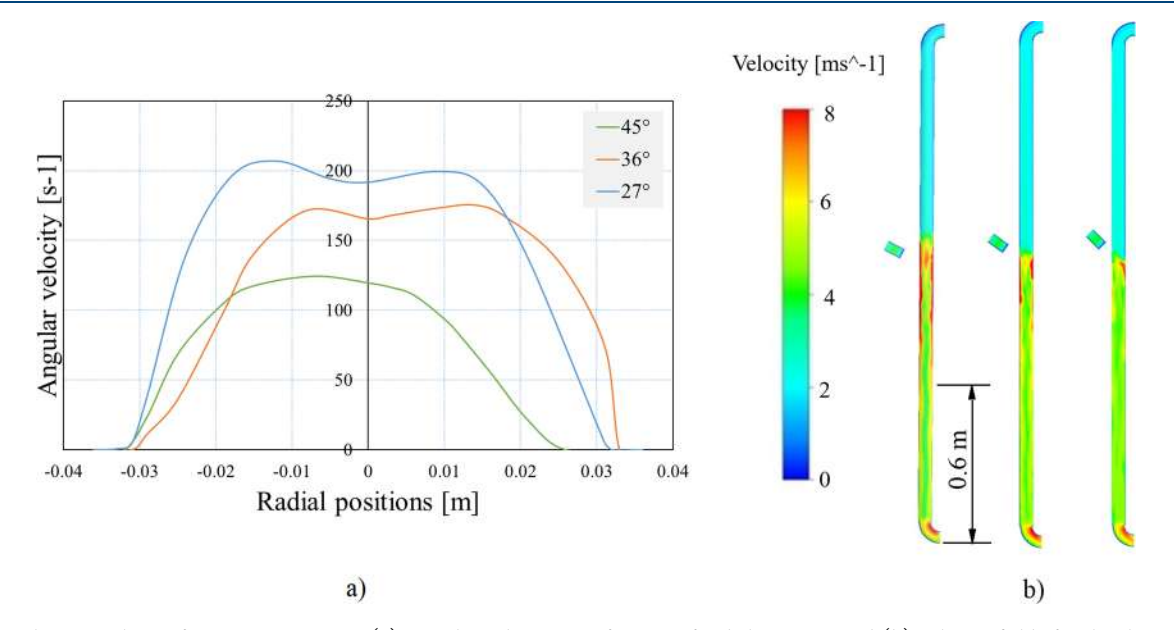


Figure 5. Velocity analysis of air—water mixture. (a) Angular velocity as a funtion of radial position and (b) velocity fields for the three proposed geometries.

result of the sudden change of velocity experimented with the inlet stream when it clashes with the walls to form the swirl flow. This sudden change is more intense when the angle is lower. As a result of that, for the inlet with an angle of 27°, the pressure drop is up to 1.6 and 3.5 times higher than those of the others, respectively.

Figure 7 shows the profile and contour of the liquid volumetric fraction, as well as the liquid mass flow fields for all of the inlet angles. The volumetric fraction profile (Figure 7a)

is measured in the radial position at a height of 0.6 m from the bottom of the separator. It is possible to observe the liquid adhesion in the GLCC walls, which is the two-dimensional representation of the vortex formation corresponding to phase separation by the action of centrifugal force. Apparently, the three inlet angles have an adequate vortex formation. However, the water mass flow fields show that for the 27° inlet angle there is liquid carry-over, which could generate operational problems downstream.

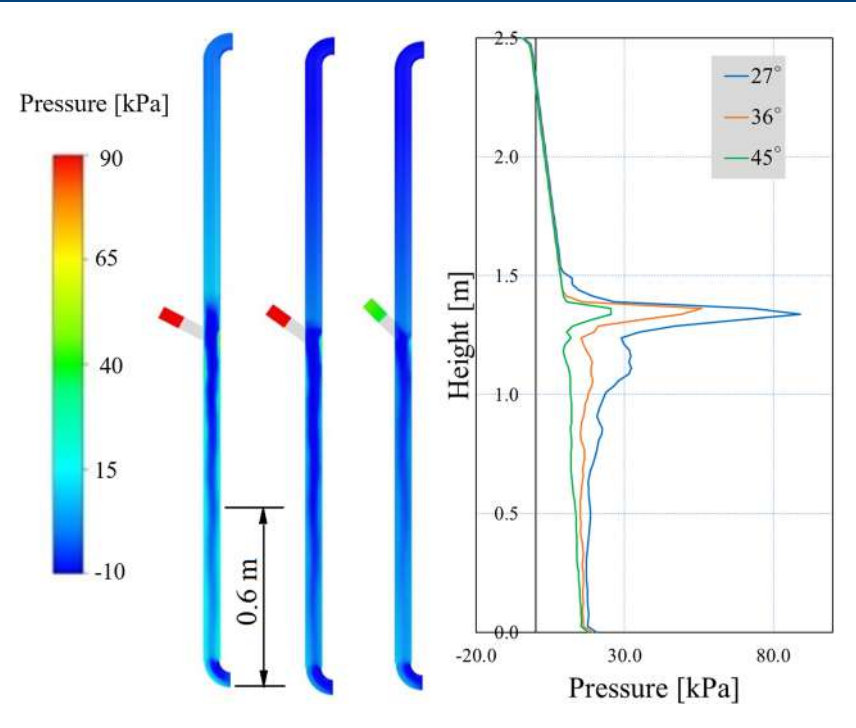


Figure 6. GLCC pressure drop for an air-water mixture.

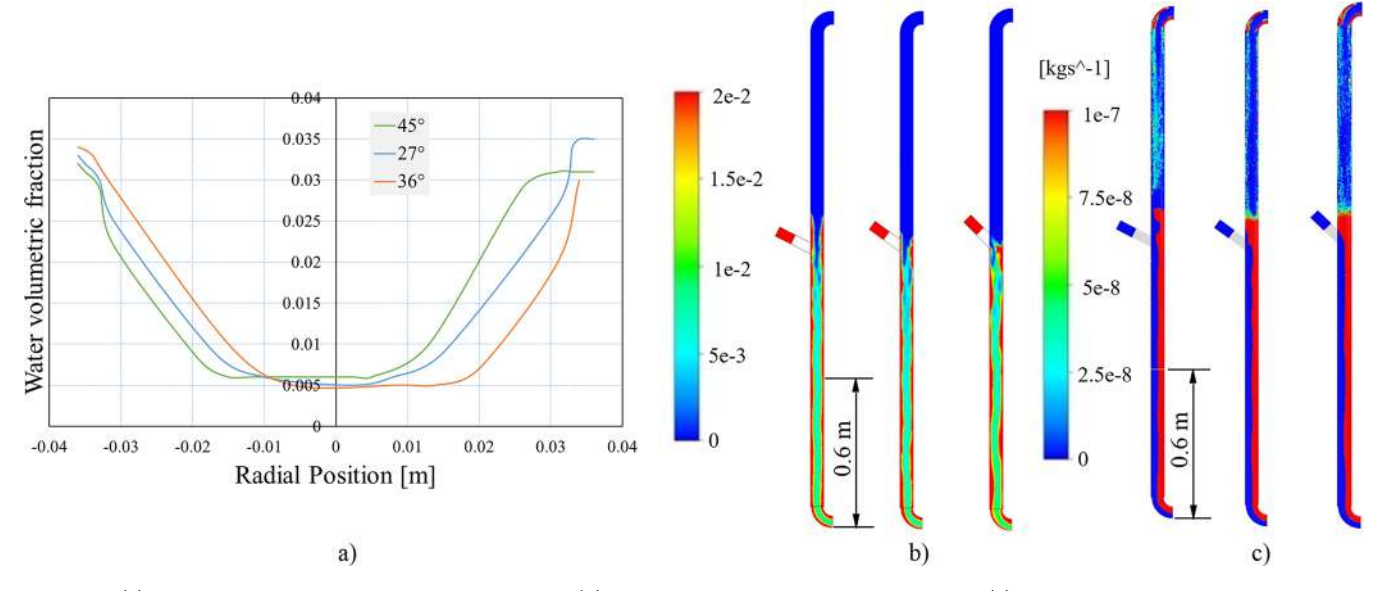


Figure 7. (a) Water volumetric fraction vs radial position. (b) Fields of water volumetric fraction and (c) water mass flow.

In addition to the validation of the multiphase model for the air—water mixture in a GLCC separator, the effect of the separator geometry was analyzed through the variation of the inlet nozzle angle, i.e., at 27°, 36°, and 45°. Three flow variables were analyzed, namely, the mixture angular velocity, the pressure drop, and the volumetric fraction of liquid. Considering that it is an air—water mixture at atmospheric pressure, it would be believed that there is no significant effect on the geometry of the results. However, the profiles shown in Figures 5–7 show that an increase in the inlet angle generates a decrease in the angular velocity, which is the main vortex generator within the separator. This in turn is what grants the centrifugal force as a physical principle of separation. Therefore, with the analysis of the first variable it is possible to discard the largest inlet angle to the separator. The increase

in angular velocity is accompanied, consequently, by an increase in the pressure drop inside the device (Figure 6), which could generate operational problems downstream of the separator. In the oil and gas industry losing pressure means an increase in the operating costs because it would be necessary to have more energy in the compression system to bring the gas to the transport network conditions.

Finally, the profile and contours of the volumetric fraction (Figure 7) show the liquid adhesion to the separator walls for all of the inlet angles. However, the mass flow contours reveal that for the 27° angle, there is a greater tendency to the liquid entrainment compared to the 36° and 45° inlet nozzles. In this sense, in looking for a balance between vortex formation, pressure drop, and a decrease in entrainment, the geometry with a 36° inlet nozzle was selected for the numerical

calculations of the natural gas component behaviors inside the GLCC separator.

Colombian Natural Gas Mixture. The application of centrifugal separation to natural gas mixtures was carried out using natural gas from a Colombian field called Cusiana, which has a controlled production (December/2018) of 170 MMSCFD. The composition and physical properties are shown in Table 1. Due to the fact that the natural gas does not have completely differentiated phases depending on the components present in the mixture, the species transport model was chosen to represent the behavior of natural gas inside the GLCC separator. The angular velocity, volumetric fraction, and composition of the species were analyzed. Figure 8 shows that the swirl intensity of the natural gas can be up to 24% higher compared with the air—water mixture as a result of the low quantity of liquid.

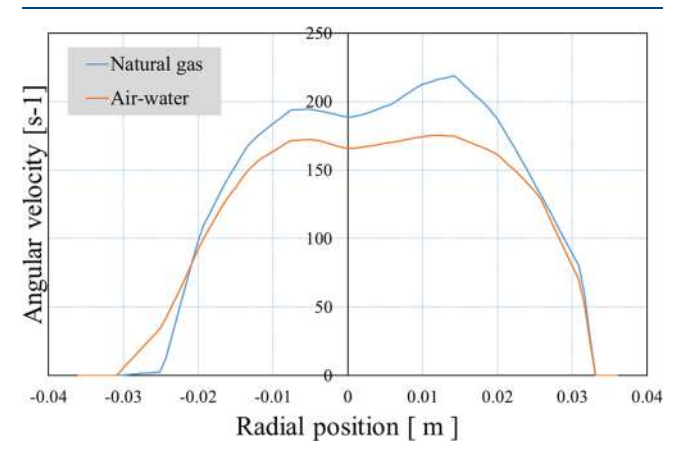


Figure 8. Comparison of angular velocity for air—water and natural gas mixtures.

The volumetric fraction contours for each substance presented in the natural gas mixture are shown in Figure 9. These contours have different scales due to the wide range of the component concentrations. In these contours, the heavier components are located at the bottom and in the separator walls by the action of the centrifugal force. It is also observed

that the lighter component, the methane, exits the separator through the upper outlet, which could be due to the amount of this component compared to the others. The small amounts of pentane and hexane reveal only a few traces of these components inside the GLCC separator.

Table 4 shows the final composition of the natural gas after the separation process; it is observed that the designed length

Table 4. Natural Gas Final Composition

	molar percent (%)		
compound	inlet	top outlet	bottom outlet
methane	82.19	100	37.75
ethane	10.43	0	35.81
propane	3.59	0	12.42
butane	1.02	0	1.86
pentane	0.12	0	0.17
hexane	0.02	0	0.07
nitrogen	0.65	0	1.48
carbon dioxide	1.97	0	10.44

is adequate because there is enough space for the USLF formation. The liquid species phase descends, and the methane rises to the top of the GLCC. It is also observed that 87% of the inlet methane comes out by the gaseous stream.

CONCLUSIONS

In this work, numerical simulations of a gas—liquid cylindrical cyclone (GLCC) separator using computational fluid dynamics (CFD) were developed. Initially an air—water mixture at atmospheric pressure and the Eulerian mixture model for the multiphase system were used; these models were validated by comparison with experimental data from the literature. Subsequently, the species transport model was used to analyze the behavior of a natural gas mixture from a Colombian field called Cusiana. The $k-\varepsilon$ turbulence model was used with standard wall functions, according to the recommendation of previous works that use CFD in GLCC separators. A mesh independence test with seven computational meshes and refining in the regions near the wall using the inflation technique was developed. Three different angles in the inlet

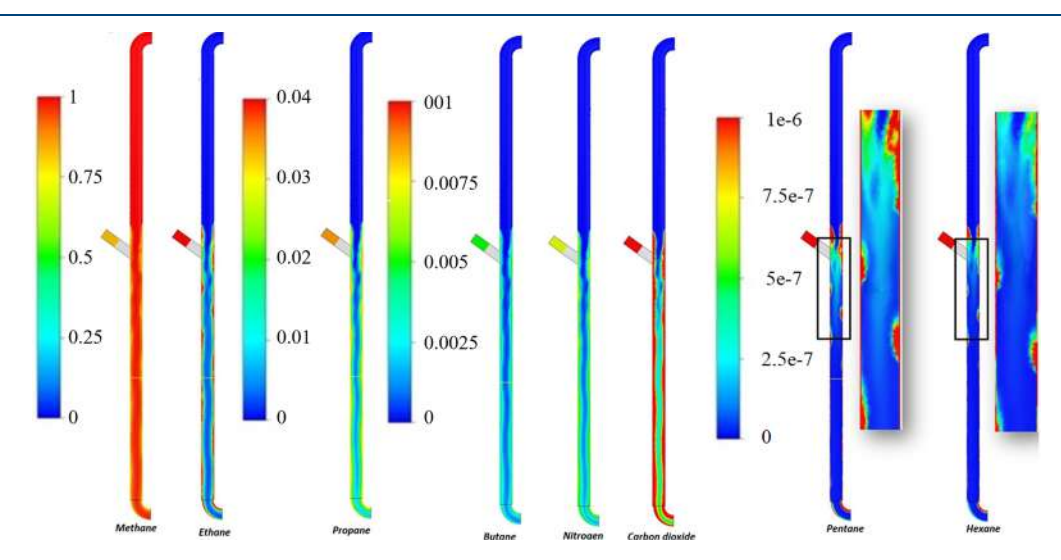


Figure 9. Volumetric fraction contour for all of the natural gas components. From left to right: methane, ethane, propane, butane, nitrogen, carbon dioxide, pentane, and hexane.

nozzle to the separator were tested to obtain a balance between the formation of the vortex corresponding to the centrifugal processes and the pressure drop inside the equipment.

The results showed that an angle of 36° at the inlet of the separator is adequate for the developing process. For the air—water mixture, the profiles and contours of velocity, pressure, and volumetric fraction showed the swirl that generates the centrifugal force to separate the phases, which also showed an adequate correlation with the experimental data. The results from applying the natural gas mixture showed that the vortex intensity was 24% higher compared to the results for the air—water mixture; the results also showed that the heavy components such as pentane and hexane are kept in the lower section of the separator and that the methane comes out from the top. However, the results make clear the need to have experimental information on the separation process of natural gas phases in the GLCC separators.

AUTHOR INFORMATION

Corresponding Author

*E-mail: natispj@gmail.com. Tel.: +57 317 3319401.

ORCID ®

Juan Sebastian Cornejo Caceres: 0000-0001-6490-3354

Natalia Prieto: 0000-0001-9178-7758 German Gonzalez: 0000-0002-4642-1092

Notes

The authors declare no competing financial interest.

ACKNOWLEDGMENTS

N.P. received funding from the COLCIENCIAS national doctorates program (call 647 of 2014–2019). All of the authors thank the Industrial University of Santander for academic support.

SYMBOLS LIST

 $C_{1\varepsilon}$, $C_{2\varepsilon}$, $C_{3\varepsilon}$ = turbulence model constants

 D_t = turbulent diffusivity

E =empirical constant

 \vec{F} = additional external body forces

 $G_{\rm b}$ = generation of turbulence kinetic energy due to buoyancy

 G_k = generation of turbulence kinetic energy due to the mean velocity gradients

 \vec{I} = identity tensor

 J_i = diffusion flux of species i

 $J_{i,w}$ = diffusion flux of species i at the wall

 $\overrightarrow{k_p}=$ turbulence kinetic energy at the wall-adjacent cell centroid

N = total number of species

 S_{ε} , S_k = source terms

 Sc_t = turbulent Schmidt number

 \vec{T} = viscous stress tensor

 U^* = dimensionless velocity

 U_p = mean velocity of the fluid at the wall-adjacent cell centroid

 Y_i = local mass fraction of each species

 $Y_{\rm M}$ = contribution of the fluctuating dilatation in compressible turbulence to the overall dissipation rate

 \vec{a} = secondary phase droplet's acceleration

d = diameter of the droplets of secondary phase

 $f_{\text{drag}} = \text{drag function}$

 \vec{g} = gravitational force

 \vec{k} = turbulent kinetic energy

p = static pressure

 $\vec{v}_{\text{dr},k}$ = drift velocity vector

 \vec{v}_m = average mass velocity vector

 $\vec{v}_{p,q} = \text{slip velocity vector}$

 y^* = dimensionless distance from the wall

 $y_{\rm p}$ = distance from the centroid of the wall-adjacent cell centroid

 α_k = volumetric fraction

 ε = dissipation of turbulent energy

 κ = von Kármán constant

 μ = dynamic viscosity

 $\mu_{\rm t}$ = turbulent viscosity

 ρ_m = average specific mass

 σ_{ε} = turbulent Prandtl number for ε

 σ_k = turbulent Prandtl number for k

 τ_n = particle relaxation time

REFERENCES

- (1) Shoham, O.; Kouba, G.; et al. State of the art of gas/liquid cylindrical-cyclone compact-separator technology. *JPT, J. Pet. Technol.* **1998**, *50*, 58–65.
- (2) Wang, S.; Gomez, L. E.; Mohan, R. S.; Shoham, O.; Kouba, G. E. Gas-Liquid Cylindrical Cyclone (GLCC©) Compact Separators For Wet Gas Applications. *J. Energy Resour. Technol.* **2003**, *125*, 43–50.
- (3) Hoffmann, A.; Stein, L. Gas Cyclones and Swirl Tubes: Principles, Design, and Operation 2008, 1–422.
- (4) Kouba, G.; Wang, S.; Gomez, L.; Mohan, R.; Shoham, O. Review of the state-of-the-art gas-liquid cylindrical cyclone (GLCC) technology-field applications. *International Oil and Gas Conference and Exhibition in China* **2006**, 1.
- (5) Kouba, G. E.; Shoham, O.; Shirazi, S. Design and performance of gas-liquid cylindrical cyclone separators. In *Proceedings of the BHR Group 7th International Meeting on Multiphase Flow*, June 7–9, 1995, Cannes, France; BHR Group: 1995; pp 307–327.
- (6) Kouba, G.; Shoham, O. A Review of Gas-Liquid Cylindrical Cyclone (GLCC) Technology. In *Proceedings of the Production Separation Systems International Conference*, April 23–24, 1996, Aberdeen, England; Chevron Petroleum Technology Company and The University of Tulsa: 1996.
- (7) Yang, J.; Zhang, X.; Shen, G.; Xiao, J.; Jin, Y. Modeling the mean residence time of liquid phase in the gas—liquid cyclone. *Ind. Eng. Chem. Res.* **2015**, *54*, 10885—10892.
- (8) Kha, H. M.; Phuong, N. N.; Nam, N. T. The effect of different geometrical configurations of the performances of Gas-Liquid Cylindrical Cyclone separators (GLCC). *ICSSE* **2017**, 646–651.
- (9) Carlos Berrio, J.; Pereyra, E.; Ratkovich, N. Computational Fluid Dynamics Modeling of Gas—Liquid Cylindrical Cyclones, Geometrical Analysis. *J. Energy Resour. Technol.* **2018**, *140*, 092003.
- (10) Yue, T.; Chen, J.; Song, J.; Chen, X.; Wang, Y.; Jia, Z.; Xu, R. Experimental and numerical study of Upper Swirling Liquid Film (USLF) among Gas-Liquid Cylindrical Cyclones (GLCC). *Chem. Eng. J.* **2019**, 358, 806–820.
- (11) Huang, L.; Deng, S.; Chen, Z.; Guan, J.; Chen, M. Numerical analysis of a novel gas-liquid pre-separation cyclone. *Sep. Purif. Technol.* **2018**, *194*, 470–479.
- (12) Vieira, R.; Sajeev, S.; Shirazi, S.; McLaury, B.; Kouba, G. Experiments and Modelling of Sand Erosion in Gas-Liquid Cylindrical Cyclone Separators Under Gas Production and Low-Liquid Loading Conditions. In Proceedings of the 17th International Conference on Multiphase Production Technology, June 10–12, 2015, Cannes, France; OnePetro: 2015.
- (13) Ghasemi, A.; Shams, M.; Heyhat, M. M. A numerical scheme for optimizing gas liquid cylindrical cyclone separator. *Proc. Inst. Mech. Eng., Part E* **2017**, 231, 836–848.

- (14) Gomez, L. E.; Mohan, R. S.; Shoham, O.; Marrelli, J. D.; Kouba, G. E. State-of-the-art simulator for field applications of gasliquid cylindrical cyclone separators. SPE ATCE 1999, 1.
- (15) Gomez, L.; Mohan, R.; Shoham, O.; Kouba, G.; et al. Enhanced mechanistic model and field-application design of gas/liquid cylindrical cyclone separators. SPE J. 2000, 5, 190–198.
- (16) Elsayed, K.; Lacor, C. The effect of cyclone inlet dimensions on the flow pattern and performance. *App Math Model* **2011**, *35*, 1952–1968.
- (17) Arpandi, I.; Joshi, A. R.; Shoham, O.; Shirazi, S.; Kouba, G. E.; et al. Hydrodynamics of two-phase flow in gas-liquid cylindrical cyclone separators. *SPE J.* **1996**, *1*, 427–436.
- (18) Hreiz, R.; Lainé, R.; Wu, J.; Lemaitre, C.; Gentric, C.; Fünfschilling, D. On the effect of the nozzle design on the performances of gas—liquid cylindrical cyclone separators. *Int. J. Multiphase Flow* 2014, 58, 15–26.
- (19) Drew, D. A. Mathematical modeling of two-phase flow. *Annu. Rev. Fluid Mech.* **1983**, *15*, 261–291.
- (20) Crowe, C. T.; Schwarzkopf, J. D.; Sommerfeld, M.; Tsuji, Y. Multiphase Flows with Droplets and Particles 2011, 1.
- (21) Manninen, M.; Taivassalo, V.; Kallio, S. On the Mixture Model for Multiphase Flow; VTT Publications: 1996.
- (22) Schiller, L.; Naumann, A. A Drag Coefficient Correlation. Zeit Ver Deutsch Ing 1935, 77, 318–320.
- (23) Hreiz, R.; Gentric, C.; Midoux, N. Numerical investigation of swirling flow in cylindrical cyclones. *Chem. Eng. Res. Des.* **2011**, *89*, 2521–2539.
- (24) Erdal, F. M. Local measurements and computational fluid dynamics simulations in a gas-liquid cylindrical cyclone separator. Ph.D. Thesis, University of Tulsa, 2001.
- (25) Versteeg, H. K.; Malalasekera, W. An Introduction to Computational Fluid Dynamics: The Finite Volume Method, 2nd ed.; Pearson Education Ltd.: 2007.
- (26) Wilcox, D. C. Turbulence Modeling for CFD; DCW Industries: La Canada, CA, 1998; Vol. 2.
- (27) Launder, B. E.; Spalding, D. B. Numerical prediction of flow, heat transfer, turbulence and combustion 1983, 96–116.
- (28) Amell, A. A.; Bedoya, C. A.; Suárez, B. Efectos del cambio de composición química del gas natural sobre el comportamiento de turbinas a gas: Una aproximación al caso colombiano. *Energética* **2006**, 35, 23–31.
- (29) Patankar, S. Numerical Heat Transfer and Fluid Flow; CRC Press: 1980.